Supporting Information

Hajj et al. 10.1073/pnas.1412396111

SI Text

3D Reconstruction and Localization Algorithm. Throughout this study, 3D Gaussian fitting was used to localize molecules based on the methods reported in ref. 1.

Nine subimages were first extracted from the full image and recombined into a single z stack after correcting for any eventual magnification difference, rotation, or translation (as described previously in ref. 2). The images were then smoothed using a Gaussian filter, and points above a certain threshold were marked as potential candidates. Around each candidate, a 3D box was taken, and the background amplitude was estimated. The 3D intensity profile was then fitted to a 3D integrated Gaussian profile, which takes into consideration the pixelization effect of the detector. The fitting was implemented in Matlab using the built-in function erf. The signal was fitted using the lsqcurvefit function to the following function $Amp\times\iiint e^{-(x-x_0/\sigma_x\sqrt{2})^2}e^{-(y-y_0/\sigma_y\sqrt{2})^2}e^{-(z-z_0/\sigma_z\sqrt{2})^2}dxdydz+bgd$ over all of the pixels, with the integral being over each of the voxels, Amp representing the amplitude, and bgd representing the background. The 3D position (x_0,y_0,z_0) was then estimated as well as the SD of the Gaussian $(\sigma_x,\sigma_y,\sigma_z)$.

The fitting parameters, such as the different σ, were chosen to be free. To illustrate the advantage of free-fitting parameters, images of fluorescent beads on a cover glass were acquired while displaced over the whole axial range of observation. The positions of the beads were determined by 3D Gaussian fitting with either free-fitting or fixed parameters. The fixed parameters were found by fitting the PSF of a representative bead sample and evaluating the average values of the σ. Later, the fitting parameters were fixed to be within a band of 2 × SD in the width around the mean value. The two methods offered similar results for the localization precision, with a slight advantage for free-fitting parameters near the edges as illustrated in Fig. S1. Accordingly, all of the parameters were chosen to be free during the localization process.

During data analysis, the detected points were further filtered according to the fitting parameters, such as the width of the Gaussian, the amplitude, and the fit quality, to rule out possible false positives or poor-quality detections. It was also necessary to delete a few of the detections outside the imaged volume, because they are expected to be of a lower precision quality. The filtering was done using a custom MATLAB code while observing the resultant image.

Determining the Number of Photons and Accuracy. Pixel intensity values of EM–CCD cameras can be converted to a number of photons through multiplication by a conversion factor specified by the manufacturer of each camera. A first approach to determine the photon count is integrating the area under the Gaussian profile obtained from the fitting. However, because the images at the output of the MFM are multiplied by an intensity correction factor as previously described, the simple integral will result in an overestimation of the number of photons. For this reason, photon counts were estimated by pixel intensity values of the raw images.

After localization, the unfiltered raw image was imported and overlaid with the localizations. Around each point, the pixel intensity values of a 3D voxel of $2\cdot\sigma\_x\times2\cdot\sigma\_y\times2\cdot\sigma\_z$ was summed after removing the constant offset of the camera.

The accuracy was then estimated for different spacing between planes (Fig. S2) by imaging stationary fluorescent beads over 100 frames. Although σ_x and σ_y of the microscope PSF induced the same pixel number in xy for all of the gratings as the total magnification was fixed, the number of pixels along z for smaller grating spacing was greater, resulting in a higher detected number of photons and better localization accuracy (Fig. S2). The accuracy of each localization was estimated as

$$\left\langle(\Delta x_i)^2\right\rangle=\frac{\sigma_i^2+a_i^2/12}{N}+\frac{4\sqrt{\pi}\sigma_i^3b^2}{a_iN^2},$$

where i stands for the dimension (3, 4), a is the pixel size, and N is the number of photons involved in the fitting. Fig. S2 shows the accuracy as a function of the number of photons for different plane spacing.

IR Stabilization. To correct for any possible drift in the sample during acquisition, we implemented a very precise localization technique using the diffraction pattern of a polystyrene bead. We use an IR LED (M780L2) to illuminate the bead without interfering spectrally with the excitation or emission of the sample. A dichroic mirror is placed on the emission path to reflect the IR light that forms a transmission image on a different camera (JAI-CV-A50IRE). The shape of the diffraction ring is analyzed separately with a home-built C code to infer the localization of the bead in time. We followed the same principle as reported in ref. 5 and adapted it to our use. Hereafter, we recall the main principle.

IR light diffracted by the 4-μm bead appears as concentric dark and bright rings, and the position, radius, and relative intensity depend on the precise position of the beads along the optical axis. Those rings can be used to extract the exact z position of the bead and follow any sample drift.

The beads were added to the sample, washed to remove nonadherent ones, and then, imaged with IR. The symmetry of the diffraction rings is a key feature to find the precise central position of the bead. A region of 128 × 128 pixels was taken around the bead. Pixels were averaged over 10 pixels from the central x and y axes of this area. The intensity profile must be symmetric around the center position of the bead, and the average profile $I(x+\delta x)$ should be equal to $I(-x-\delta x)$. To determine δx, one can compute the correlation function $C(t)=I(x)\times I(-x+t)$, in which maxima should occur at $t=2\delta x$. This method offers a reliable method to localize the center of the beads. After the center position is found, average values of the pixels within a circular band of an increasing radius were recorded in a table. This calculation was repeated while moving the piezostage with known axial steps and recording this table for each position. Consequently a calibration table was created that can be used later during imaging to compute the exact z position.

During superresolution data acquisition, the IR bead image was used to find the x, y position, and the ring intensity variation was compared with the calibration table to extract the exact z position of the bead/slide using polynomial interpolation.

The code for IR camera acquisition as well as calibration and tracking was implemented in C language and could go as fast as 30 Hz. Although the code can be used to stabilize the sample holder directly if an adequate stage is available; we opted to use it as a postprocessing drift correction. The IR camera was synchronized externally with the imaging camera, and each frame position in 3D space was recorded. Another calibration step was carefully implemented to find the appropriate spatial coordinate transformation from IR camera to fluorescence imaging camera. Micrometer beads were mixed with 200-nm fluorescent beads inside an agarose gel, which forms a stable matrix and ensures fixed distances between the beads. An effort was made to find a region that had a fluorescent bead as well as a micrometer bead nearby. Using the microscope mechanical stage, an x, y scan was performed, covering a given grid dimension while acquiring 20 fluorescent images at each position and recording the corresponding IR images. The beads were then localized on the fluorescence image and compared with the IR recording. A Matlab code was implemented using the tform method to find the exact transformation matrix from one coordinate system to the other. This matrix was later used to correct for any recorded drift during the experiment.

Fig. S5 shows the principle of this technique as well as the step localization while z scanning. The SD of the localization is estimated to be <1 nm in the lateral dimension and <5 nm in the axial one (Fig. S6). To illustrate the drift correction performance in the imaging configuration, we used fluorescent beads embedded in an agarose gel in the vicinity of a magnetic bead. We acquired in parallel the fluorescence image using the MFM and recorded the diffraction ring image in the IR channel. Fig. S7 shows the drift-corrected localizations recorded over 5,000 frames.

Spacing and Imaging Wavelength Influence. MFM is based on the introduction of an MFG in the back focal plane of an imaging objective. To image multiple axial planes simultaneously, the grating is chirped to induce different defocusing powers in the different diffraction orders.

A major characteristic of a grating is the ability to separate light in function of its wavelength. In the MFM, this property introduces a lateral chromatic aberration, which is corrected using a combination of blazed grating and prism. Axial aberration, which originates from the grating design and material dispersion, needs also to be accounted. The MFG grating is optimized, such that the wavefront of light waves emanating from emitters at specific positions along the optical axis would be corrected. The sine condition indicates that the wavefront of an emitter at a position Δz from the objective focal plane has a phase shift at the back focal plane of

$$\Delta\varphi = \frac{2\pi}{\lambda} n \Delta z \sqrt{1-\sin(\theta)^2}.$$

Here, n is the index of refraction, λ is the imaging wavelength, and θ is the angle of incidence.

The design of the grating is based on a distortion of the periodic structure of a regular grating in the lateral directions (x and y) to compensate for this phase shift. The distortion along the x direction follows the equation

$$\delta x_d = n_{\lambda_d} \frac{d}{\lambda_d} \Delta z_d \sqrt{1-\frac{x^2+y^2}{\left(n_{\lambda_o} f_{obj}\right)^2}},$$

where n_{λ_d} is the index of refraction at the design wavelength λ_d, d is the period, f_{obj} is the objective focal distance, and (x,y) are the coordinates at the pupil plane. The distortion on the y direction is chosen to $\delta y = N \times \delta x$ ($n = 3$ in our case). The total phase shift is

$$\begin{aligned}\Delta\Phi_d = \delta\phi_x + \delta\phi_y &= \frac{2\pi}{d}\left(m_x + N m_y\right)\delta x_d \\ &= \frac{2\pi}{\lambda_d} n_{\lambda_d}\left(m_x + N m_y\right)\Delta z_d \sqrt{1-\frac{x^2+y^2}{\left(n_{\lambda_o} f_{obj}\right)^2}}.\end{aligned}$$

It is important to note the following facts. First, the diffraction order (m_x, m_y) corrects for a wavefront emerging from a plane at $-(m_x + N m_y)\Delta z$ (if imaged with the same wavelength). Second, this resultant phase shift is proportional to the fixed lateral distortions of the grating. Third, the distortion and thus, the phase shift of the different orders are inversely proportional to the wavelength of the imaging light. Imaging at a different wavelength with the same grating distortion, thus, affects the phase profile for which the correction is happening.

When imaging at a different wavelength ($\lambda' \neq \lambda$), the phase-shift profile at the back focal plane of the imaging objective of an emitter placed at $\Delta z'$ along the optical axis has the following form:

$$\Delta\Phi' = \frac{2\pi}{\lambda'} n_{\lambda'} \Delta z' \sqrt{1-\frac{x^2+y^2}{\left(n_{\lambda'_o} f_{obj}\right)^2}}.$$

To be corrected, this phase should match the one induced by the grating but with opposite sign ($\Delta\Phi_d = -\Delta\Phi'$), which can be written more explicitly as

$$\frac{2\pi}{\lambda'} n_{\lambda'} \Delta z' \sqrt{1-\frac{x^2+y^2}{\left(n_{\lambda'_o} f_{obj}\right)^2}} = -\frac{2\pi}{\lambda_d} n_{\lambda_d}\left(m_x + N m_y\right)\Delta z_d \sqrt{1-\frac{x^2+y^2}{\left(n_{\lambda_o} f_{obj}\right)^2}}.$$

As such, the resulting spacing between two consecutive planes can be expressed as

$$\Delta z' = \Delta z_d \frac{\lambda'}{\lambda_d} \frac{n_{\lambda_d}}{n_{\lambda'}} \frac{\sqrt{1-\frac{x^2+y^2}{\left(n_{\lambda_o} f_{obj}\right)^2}}}{\sqrt{1-\frac{x^2+y^2}{\left(n_{\lambda'_o} f_{obj}\right)^2}}}.$$

We note that the spacing is linearly proportional to the imaging wavelength, with an additional proportionality factor depending on the dispersion. The second factor is usually negligible, and the main contribution arises from the wavelength. Fig. 3 shows the spacing recorded for three different colors, and Fig. 3*D*, *Inset* shows the linear dependency of the spacing over the wavelength in accordance with the theory prediction.

This effect will show up on the PSF as a small broadening of the axial profile, which will be limited by the filter bandwidth. This broadening effect will be more pronounced when moving away from the nominal focal plane of the microscope. Although a filter of 30-nm bandwidth will reduce this effect, sequential acquisition with two well-separated colors would be more affected. A calibration step is, thus, necessary to find the corresponding spacing and enable a correct coregistration.

Experimental Assessment of Localization Precision. The final resolution of superresolution images using the MFM may be influenced by many factors, mainly the number of emitted photons per molecule (which influences the localization precision) and the axial position of the molecule. To efficiently isolate the influence of the z position on the resolution, we fixed the number of the emitted photons by imaging the same subdiffraction beads at different heights over time, assuming minimal bleaching of the beads. The SD of localizations was used as a metric to assess the influence of the imaging depth over the resolution (Fig. 3). An additional influence arises from the index of the refraction layer between the cover glass and the molecule as well as the varying number of photons emitted per molecule.

To quantify the precision and resolution in the context of cellular imaging, it is possible to isolate detections that were generated from the same molecule appearing in a few consecutive frames. As the sample is fixed, these localizations represent repeated measurements of the same position. The SD of the localizations is reported as a function of the axial position for the mitochondria sample in Fig. S8. We measured 16 nm average SD for the lateral localization and 35 nm axially. Those values are found to be homogenous over the detectable axial range, meaning that resolution is maintained over the whole imaging depth.

Data Visualization. Localizations were then imported to a custom-made visualization software ViSP (6), a freely available software tool for rendering 3D localizations. Below is a description of the relevant features that were used.

Density calculation. Densities are calculated for each localization. A sphere of user-specified radius (neighbor radius) is defined at the (*x*, *y*, *z*) position of the localization. The density is defined as the total number of localizations located within this sphere (i.e., the neighboring localizations). For the figures presented, the sphere radius is set at 100 nm. Localizations may eventually be filtered based on the assigned density metric. Because spurious localizations typically have a low density, they may be greatly suppressed by filtering in this manner.

Surface rendering. The 3D surfaces are rendered using the Marching Cubes algorithm, which renders a closed surface around a scalar field. Effectively, the density of localizations is used to represent the required scalar field, after which a surface is rendered. A smoothing operation is typically applied to reduce jaggedness in initially rendered surfaces.

Localization density profiles. Cylinders with user-specified radii along arbitrary axes are defined along which localizations can be counted and tabulated to generate 3D spatial histograms. This feature is used to show the hollowness of mitochondria in Fig. 4 *F* and *G*.

Sample Preparation.

Substrate preparation. Quality and cleanness of the substrate are major issues during superresolution imaging, because they might introduce a considerable amount of background during data acquisition. PIRANHA solution [a mixture of 3:1 sulfuric acid to 30% (wt/wt) hydrogen peroxide solution] was used to remove any organic residual.

Labeling. HeLa cells were grown in DMEM low-glucose medium. Cells were plated on clean coverslips 24 h before fixation. The fixation and labeling protocol was inspired by the study in ref. 7. Cells were washed two times with phosphate-buffered saline (PBS) and then incubated at 37 °C with 4% (vol/vol) PFA. Thoroughly washing with PBS was carried out before adding Triton X-100 (T8787; Sigma) at 0.5% in PBS for 10 min. Cells were washed with PBS and then incubated with the blocking buffer [0.1% Tween 20 in PBS (PBST)/1% BSA (A7906; Sigma) /4% (vol/vol) horse serum (008–000-121; Jackson Immune Research)] for 30 min.

Immunofluorescence labeling. Primary antibodies were dissolved at different concentrations in the blocking buffer and incubated for 60 min at room temperature. Then, the solution was removed, and 0.1% Tween-20 was added for 5 min in two runs. Secondary antibodies were added afterward for 60 min while protecting the sample from the light followed by two washings with 0.1% Tween-20. A final wash of PBS was performed before using the sample.

Nanobody labeling. Before adding the blocking buffer, four drops of image-it FX (I36933; Invitrogen) were added for 30 min. After blocking, the cells were incubated with adequate concentrations of the anti-GFP nanobody Alexa 647 (Chromotek-GFP-Trap protein ACT-CM-GFPTRAP) for 60 min. The nanobody was prepared following the work in ref. 8. The cells were then washed thoroughly with PBS.

Imaging buffer. Cells were then sealed in an adequate chamber in the presence of a STORM buffer. This buffer was optimized to maximize blinking of dye molecules. In the case of the two-color experiment with Alexa 647 and Alexa 568, the buffer was simply 100 mM MEA in PBS. For the one-color experiment with Alexa 647, the reducing buffer consisted of 50 mM MEA from Sigma (M6500), 30 mM glucose oxydase from Sigma (G6125-50Ku), and 33 µg/mL Catalase from Sigma (02071) in 10% (wt/vol) glucose.

Imaging conditions for Alexa 647. Images were later acquired with the wide-field excitation microscope (Nikon Ti); the image was recorded on the 3D emission path while shining a 640-nm laser light (10645/B1; Vortran Laser Technology) onto the sample through a multiband dichroic (Di01-R405/488/561/635; Semrock). The images were acquired using a CCD camera (DU-897E-CSo-#BV; Andor). The sample was bleached with high excitation power (~3.3 kW/cm^2), where the majority of the molecules switched to the dark state; lowering the excitation power to 1 kW/cm^2 enabled a few to remain blinking in the field of view. An activation laser at 488 nm (SAPPHIRE 488–500 CDRH; Coherent Sapphire) was used (~0.015 kW/cm^2) to increase the number of blinking points to achieve a constant number of activated molecules per frame (~200 detections per frame); 30,000 frames were acquired per cell. A filter (FF01-676/37–25; Semrock) was placed in front of the camera to detect only emission wavelength. The data were later processed with a multitarget tracing program described previously (9) for localization and rendering purposes.

Yeast experiment, strain preparation, incubation, labeling, and fixation. The tdEos fluorescent protein tag (10) was introduced together with the KanMX cassette at the C terminus of α-tubulin by lithium acetate-mediated transformation of the *Saccharomyces cerevisiae* diploid strain W1665, and transformants were selected on YPD-G418 plates. Fusion of the tag-coding sequence with one of two α-tubulin genes of the diploid was confirmed by detection of microtubules using wide-field microscopy (11) after photoconversion with 405-nm light (Fig. S11). For imaging, cells were grown in complete synthetic medium (CSM) containing 400 µg/mL adenine sulfate at 24 °C to OD$_{600}$ below 0.3.

Yeast cells were grown overnight and then placed on a clean microscope slide that had been coated with concavalin A. The cells were allowed to settle down for 20 min before fixation with 4% (wt/vol) PFA containing sucrose at pH 7.4. After 15 min, the cells were blocked with NH_4Cl solution for 20 min. The yeast cells were later washed thoroughly with PBS, incubated with concavalin A–Alexa 647 for 45 min, and washed with PBS to remove free dye molecules. The PBS was replaced by a solution of 100 mM MEA before imaging.

The two-color experiment was performed sequentially. First, Alexa 647 was imaged in over 20,000 frames without any activation to avoid bleaching or photoconversion of the tdEos molecules. Second, the tdEos was photoconverted to the active state and imaged using a 590 band-pass filter (Semrock) over 10,000 frames. The two-color data were then treated and reconstructed as described before.

1. Mueller F, et al. (2013) FISH-quant: Automatic counting of transcripts in 3D FISH images. *Nat Methods* 10(4):277–278.
2. Abrahamsson S, et al. (2013) Fast multicolor 3D imaging using aberration-corrected multifocus microscopy. *Nat Methods* 10(1):60–63.
3. Thompson RE, Larson DR, Webb WW (2002) Precise nanometer localization analysis for individual fluorescent probes. *Biophys J* 82(5):2775–2783.
4. Mortensen KI, Churchman LS, Spudich JA, Flyvbjerg H (2010) Optimized localization analysis for single-molecule tracking and super-resolution microscopy. *Nat Methods* 7(5):377–381.
5. Gosse C, Croquette V (2002) Magnetic tweezers: Micromanipulation and force measurement at the molecular level. *Biophys J* 82(6):3314–3329.
6. El Beheiry M, Dahan M (2013) ViSP: Representing single-particle localizations in three dimensions. *Nat Methods* 10(8):689–690.
7. van de Linde S, et al. (2011) Direct stochastic optical reconstruction microscopy with standard fluorescent probes. *Nat Protoc* 6(7):991–1009.
8. Ries J, Kaplan C, Platonova E, Eghlidi H, Ewers H (2012) A simple, versatile method for GFP-based super-resolution microscopy via nanobodies. *Nat Methods* 9(6):582–584.
9. Sergé A, Bertaux N, Rigneault H, Marguet D (2008) Dynamic multiple-target tracing to probe spatiotemporal cartography of cell membranes. *Nat Methods* 5(8):687–694.
10. Nienhaus GU, et al. (2006) Photoconvertible fluorescent protein EosFP: Biophysical properties and cell biology applications. *Photochem Photobiol* 82(2):351–358.
11. Gietz RD, Wood RA (2002) Transformation of yeast by lithium acetate/single-stranded carrier DNA/polyethylene glycol method. *Methods Enzymol* 350:87–96.

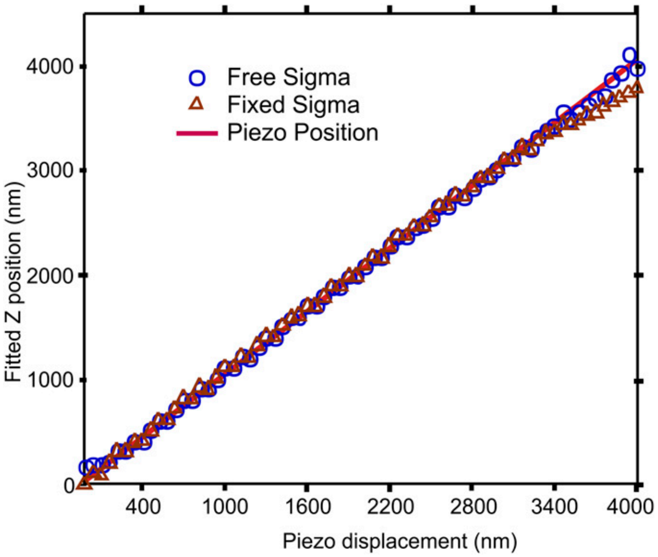

Fig. S1. Difference of fitting performance between free and fixed σ-parameters. The two methods offer good precision over the axial detection range, with slightly better performance of free-σ near the edges.

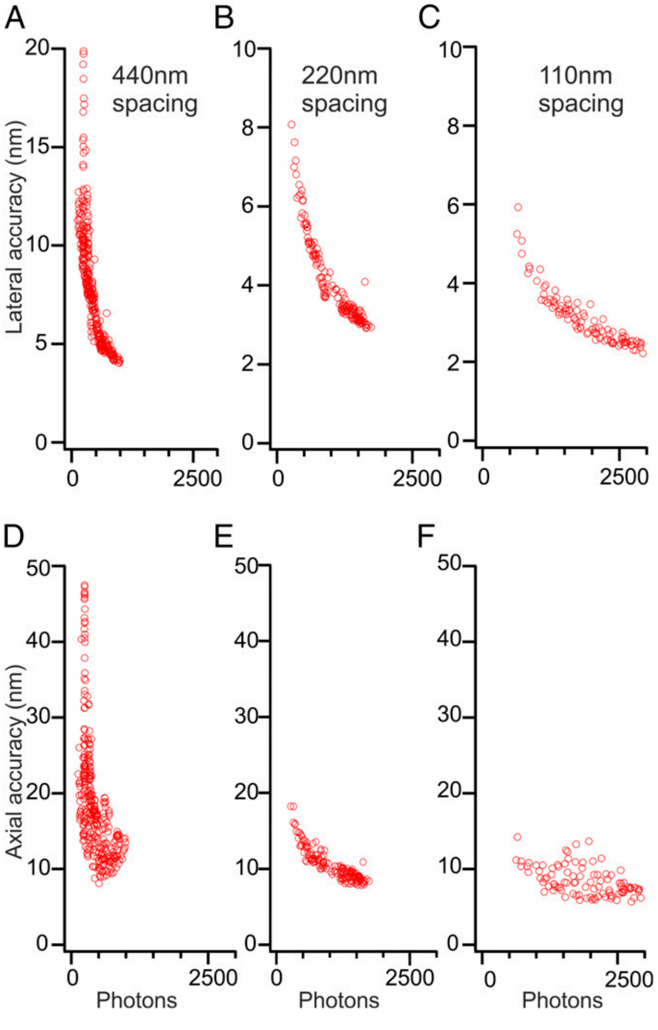

Fig. S2. Localization accuracy vs. number of detected photons with different grating combinations. (*A–C*) Lateral localization accuracy for gratings II–IV. (*D–F*) Axial localization accuracy for gratings II–IV. The spacing of 880 nm was not reported here, because it was not able to precisely locate the molecules, and the SD would not have made any sense if reported here. The typical $1/\sqrt{N}$ could be seen clearly here, and one notices the influence of better accuracy when more photons are detected.

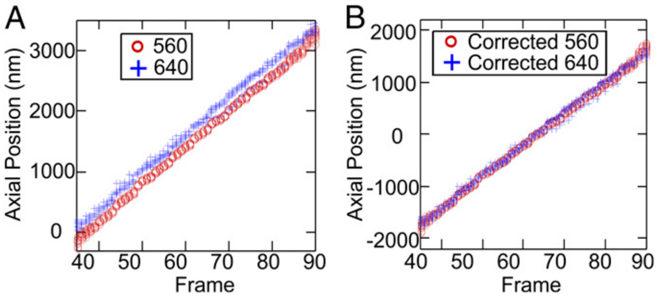

Fig. S3. Two-color registration. Calibration data of multicolor fluorescent beads taken with two different excitation wavelengths of 560 and 640 nm. (*A*) The localization of the two colors vs. the frame. (*B*) The corrected curves taking into account any misalignment or chromatic change of the focus.

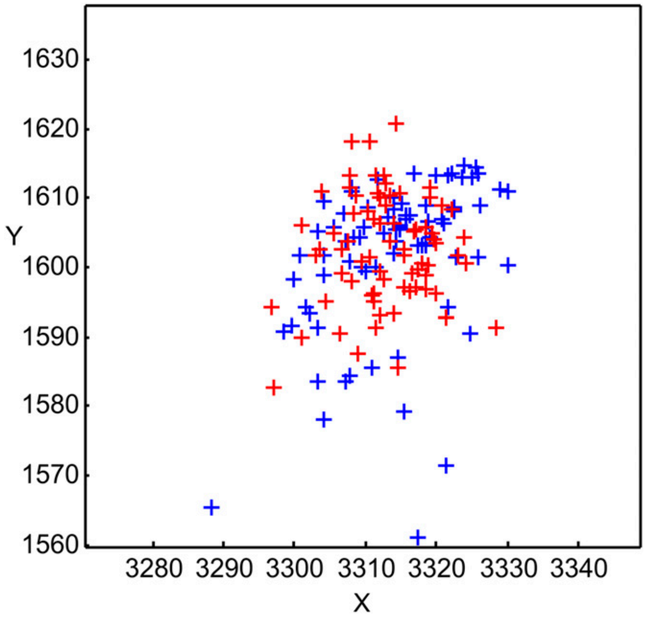

Fig. S4. Two-color lateral registration is shown to be better than 10 nm, and the axial is better than 30 nm.

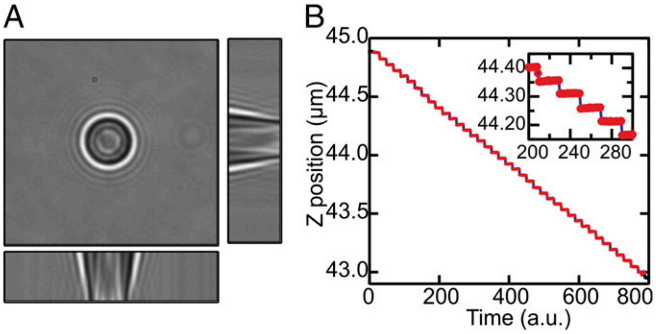

Fig. S5. Drift correction principle. (*A*) Diffraction rings of a 4-μm bead as recorded on the IR camera. (*B*) Tracking of the bead when moved at steps of 5 nm in *z* using this technique.

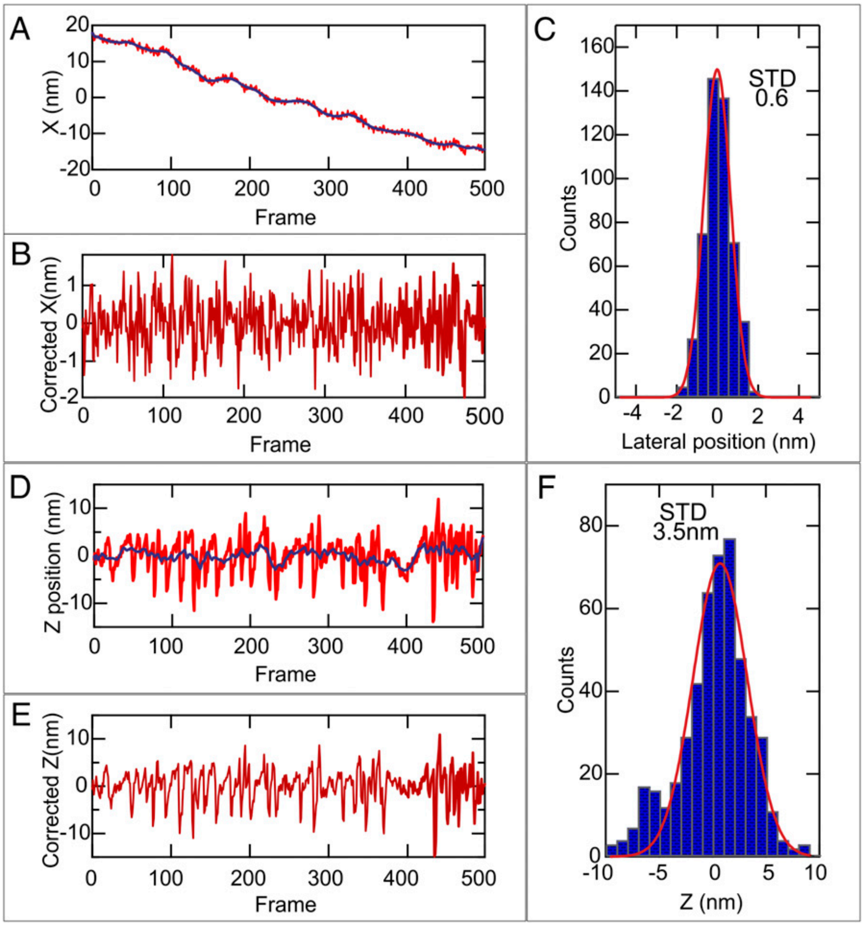

Fig. S6. Characterization of the drift correction method. (*A*) In red, lateral drift, (as recorded by the IR camera), and in blue, the smoothed values. (*B*) The corrected positions. (*C*) The histogram of lateral positions after drift correction shows a SD of 0.6 nm. (*D*) The axial drift (as recorded by the IR camera) in red, and the smoothed curve in blue. (*E*) The corrected axial positions. (*F*) The histogram of axial positions after drift correction shows a SD of 3.5 nm.

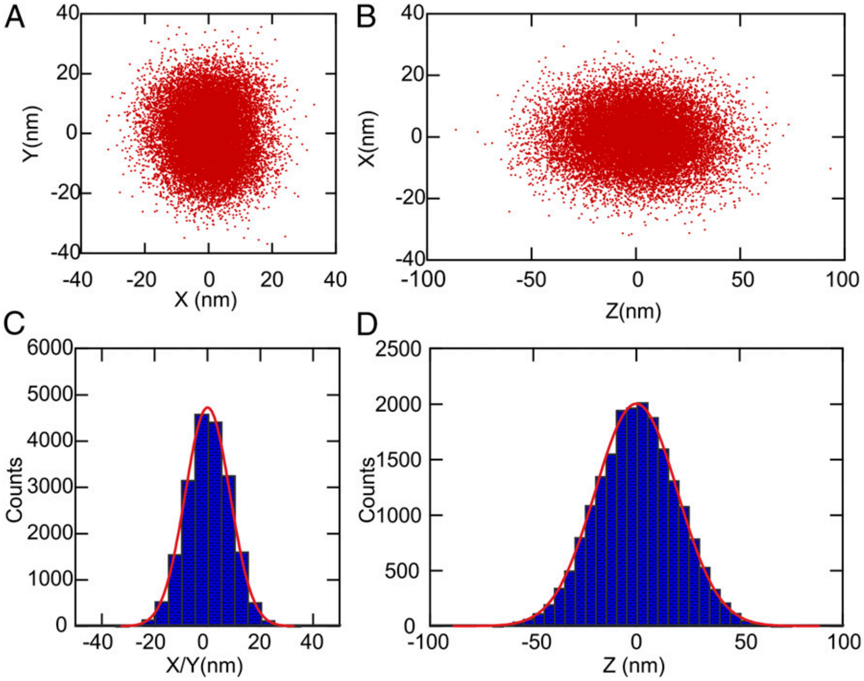

Fig. S7. Drift-corrected localization of a bead when imaged with the MFM and corrected with the diffraction ring approach. The signal-to-noise ratio of the bead was comparable with what is obtained from a single molecule. (*A* and *B*) XY and XZ projections of the drift-corrected localizations. (*C* and *D*) The corresponding histogram of lateral and axial localization.

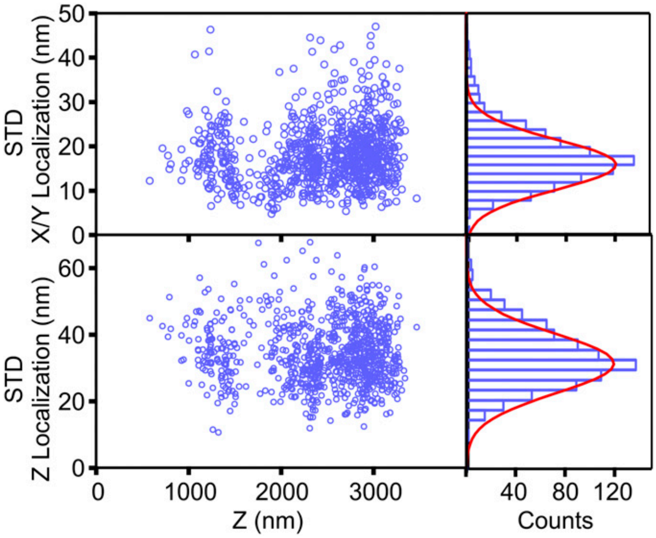

Fig. S8. Lateral and axial SDs of same molecule localizations plotted vs. the axial position. (The coverslip is located around 4,000 nm, whereas a decreasing *z* value indicates a deeper imaging inside the sample.) The data result from recording blinking molecules of Alexa 647 attached to mitochondria by nanobody labeling. (*Right*) The distribution of SDs showed an average value of 16 nm laterally and 35 nm axially.

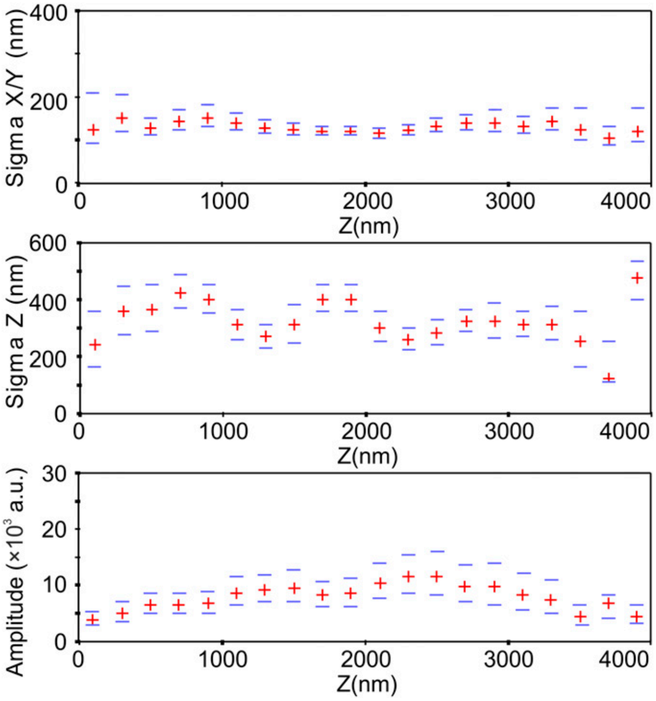

Fig. S9. The σ-distribution of the 3D Gaussian fitting averaged over 200-nm axial slices as a function of the imaging depth. The red plus signs correspond to the median value, and the blue minus signs represent the FWHM of the distribution. The detections are retrieved from the mitochondria sample labeled with Alexa 647.

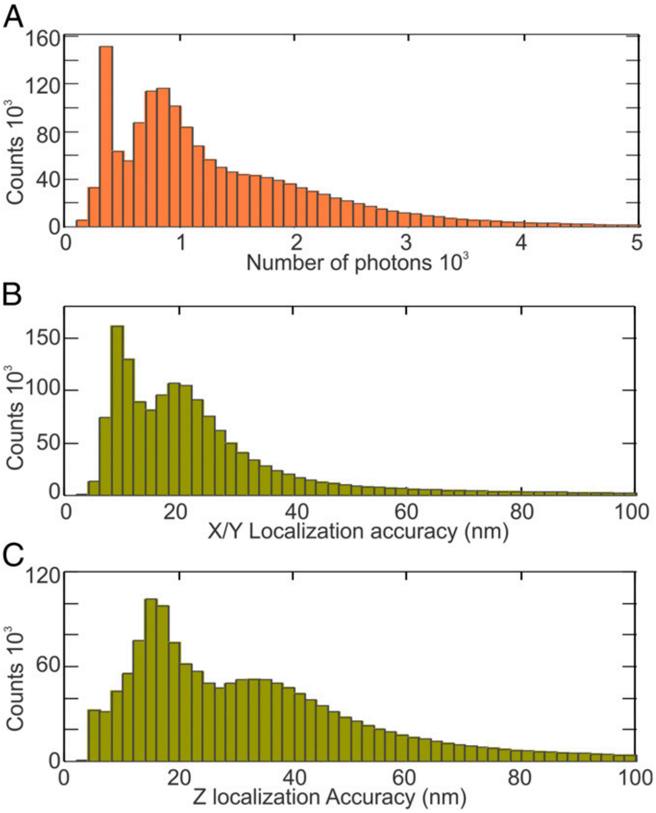

Fig. S10. Quality of localization of Alexa 647 (corresponding to Fig. 4) illustrated by (*A*) the number of photons per molecule and (*B*) lateral and (*C*) axial localization precisions. The photon count peak around 300 is caused by detections in the central plane, which are more intense than the others when imaging in the red, resulting in a greater number of photons and thus, a better localization precision.

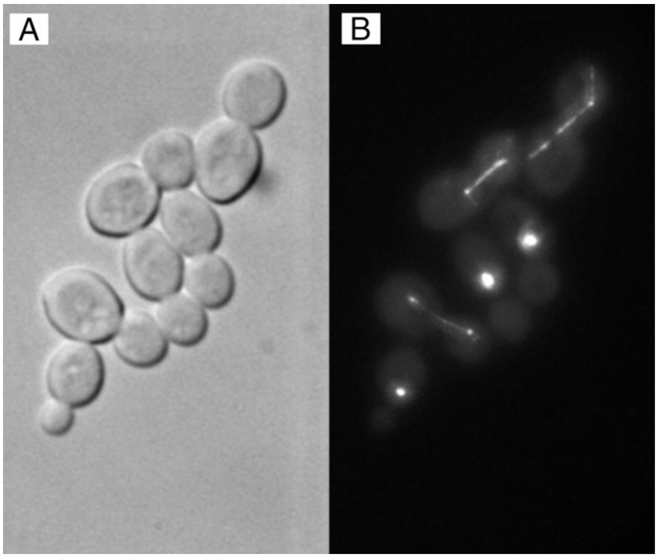

Fig. S11. Yeast cells containing tdEos-tagged α-tubulin visualized in (*A*) white light transmission and (*B*) wide-field imaging after photoconverting the tdEos protein. The tubulin fiber is clearly shown.

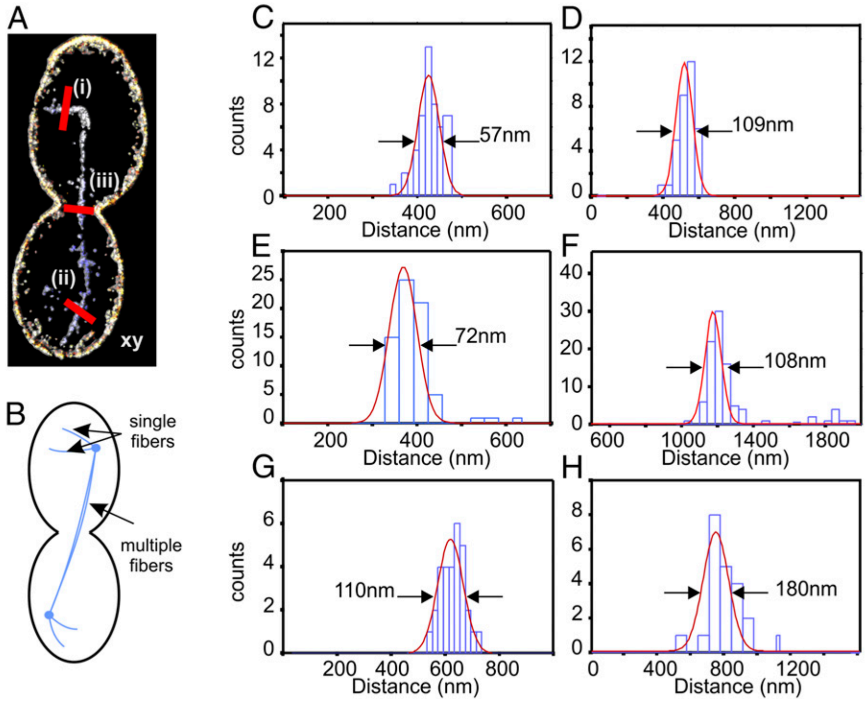

Fig. S12. Profiles of tubulin fibers at different segments. (*A*) The filtered images in different cross-sections plotted in *C*–*H* are highlighted. (*B*) Tubulin fibers are more likely to form single fibers when attached to only one centrosome and multiple fibers when attached between the two. (*C* and *D*) Lateral and axial profiles along the *i* segment. (*E* and *F*) Lateral and axial profiles along the *ii* segment. (*G* and *H*) Lateral and axial profiles along the *iii* segment. The lateral cross-sections in *i* and *ii* indicate a dimension larger than the value of 25 nm reported in ref. 26, possibly caused by the reduced localization precision in our setup and tdEos tag size.

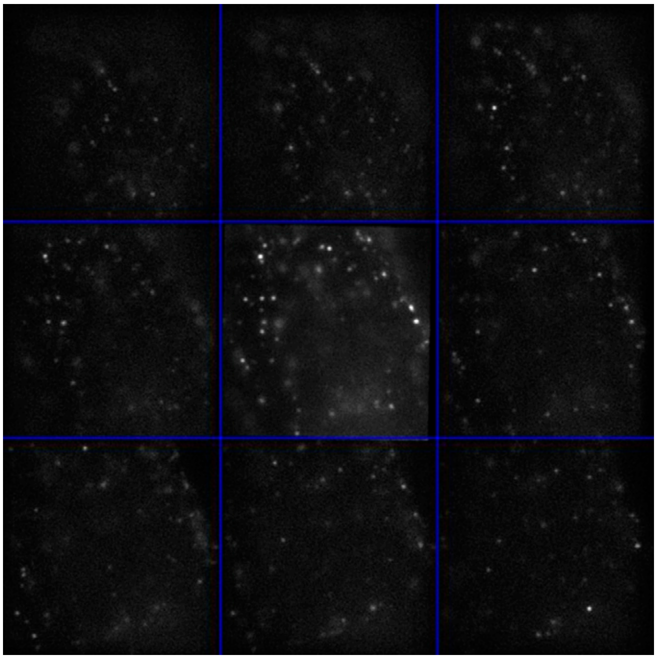

Movie S1. Example of raw images acquired using the MFM showing blinking molecules of Alexa 647 labeling the nucleopore complex in HeLa cells.

Movie S1

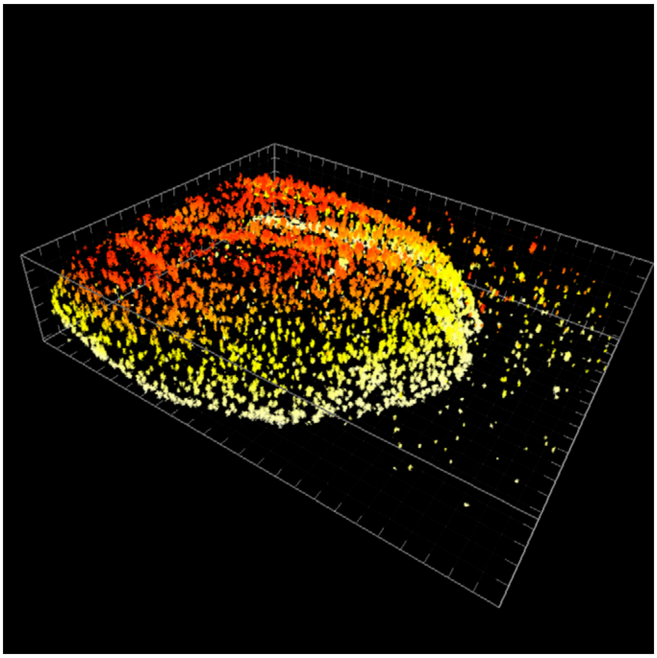

Movie S2. Reconstructed 3D superresolution volume of the raw data shown in Movie S1.

Movie S2

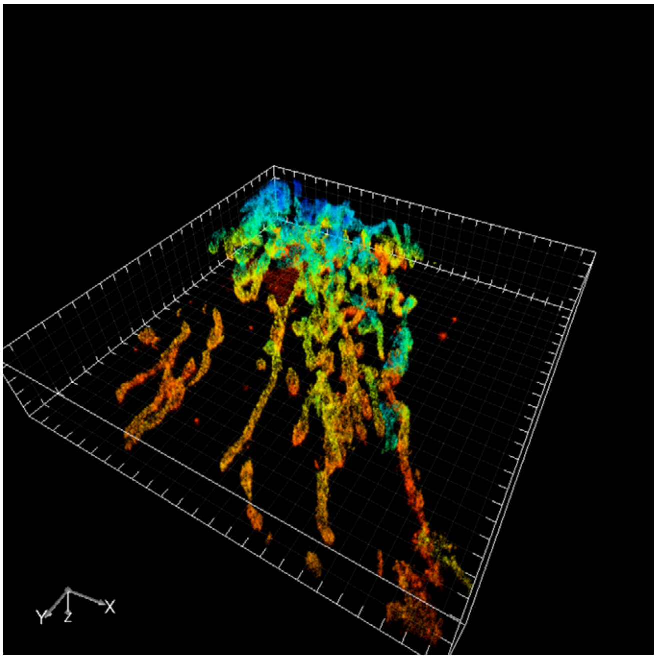

Movie S3. Reconstructed 3D superresolution volume of the mitochondrial network in HeLa cells labeled with Alexa 647 as explained in the text and corresponding to Fig. 4. The volume is rotated around the optical axis.

Movie S3

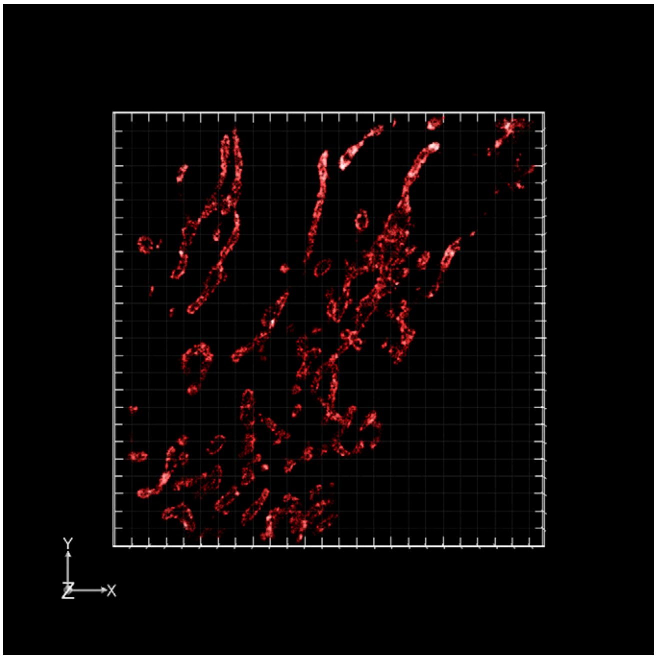

Movie S4. One hundred-nanometer section scan of the reconstructed volume along the *z* axis of the data shown in Movie S3.

Movie S4

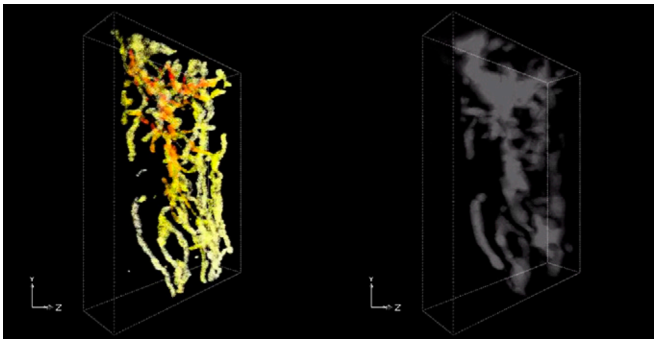

Movie S5. A comparison between the superresolution volume and the deconvolved volume of the mitochondrial network of HeLa cells.

Movie S5

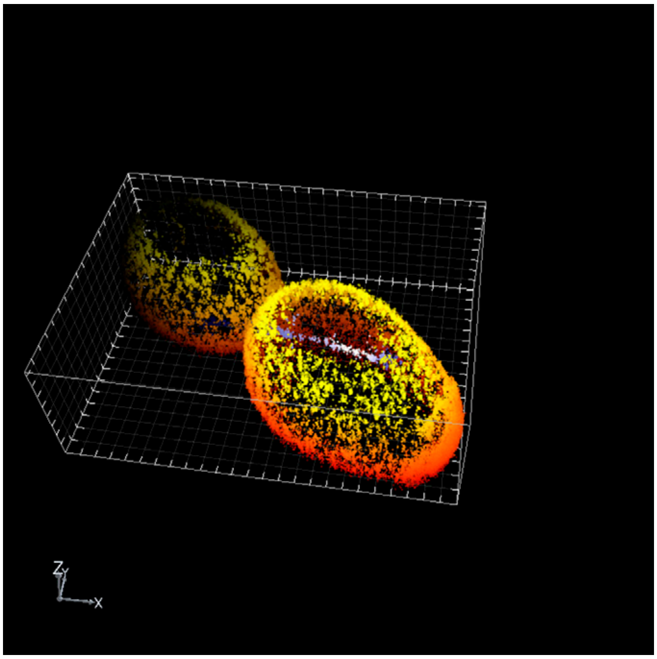

Movie S6. Reconstructed two-color 3D superresolution volume of budding yeast presented in Fig. 5*C* showing cell wall in red–orange and tubulin in white–blue.

Movie S6